

# Quantitative morphometric analysis of single gold nanoparticles by optical extinction microscopy: Material permittivity and surface damping effects

Cite as: J. Chem. Phys. 154, 044702 (2021); <https://doi.org/10.1063/5.0031012>

Submitted: 26 September 2020 . Accepted: 18 December 2020 . Published Online: 26 January 2021

 Lukas M. Payne,  Francesco Masia,  Attilio Zilli,  Wiebke Albrecht,  Paola Borri, and  Wolfgang Langbein



View Online



Export Citation



CrossMark



**New**

## Your Qubits. Measured.

Meet the next generation of quantum analyzers

- Readout for up to 64 qubits
- Operation at up to 8.5 GHz, mixer-calibration-free
- Signal optimization with minimal latency

[Find out more](#)



Zurich Instruments

# Quantitative morphometric analysis of single gold nanoparticles by optical extinction microscopy: Material permittivity and surface damping effects

Cite as: J. Chem. Phys. 154, 044702 (2021); doi: 10.1063/5.0031012

Submitted: 26 September 2020 • Accepted: 18 December 2020 •

Published Online: 26 January 2021



View Online



Export Citation



CrossMark

Lukas M. Payne,<sup>1,2</sup>  Francesco Masia,<sup>1,2</sup>  Attilio Zilli,<sup>1,3</sup>  Wiebke Albrecht,<sup>4</sup>  Paola Borri,<sup>1</sup>   
and Wolfgang Langbein<sup>2,a)</sup> 

## AFFILIATIONS

<sup>1</sup>School of Biosciences, Cardiff University, Museum Avenue, Cardiff CF10 3AX, United Kingdom

<sup>2</sup>School of Physics and Astronomy, Cardiff University, The Parade, Cardiff CF24 3AA, United Kingdom

<sup>3</sup>Department of Physics, Politecnico di Milano, Piazza Leonardo da Vinci 32, 20133 Milano, Italy

<sup>4</sup>EMAT and NANOLab Center of Excellence, University of Antwerp, Groenenborgerlaan 171, B-2020 Antwerp, Belgium

**Note:** This paper is part of the JCP Special Topic on Spectroscopy and Microscopy of Plasmonic Systems.

<sup>a)</sup>Author to whom correspondence should be addressed: langbeinww@cardiff.ac.uk

## ABSTRACT

Quantifying the optical extinction cross section of a plasmonic nanoparticle has recently emerged as a powerful means to characterize the nanoparticle morphologically, i.e., to determine its size and shape with a precision comparable to electron microscopy while using a simple optical microscope. In this context, a critical piece of information to solve the inverse problem, namely, calculating the particle geometry from the measured cross section, is the material permittivity. For bulk gold, many datasets have been reported in the literature, raising the question of which one is more adequate to describe specific systems at the nanoscale. Another question is how the nanoparticle interface, not present in the bulk material, affects its permittivity. In this work, we have investigated the role of the material permittivities on the morphometric characterization of defect-free ultra-uniform gold nanospheres with diameters of 10 nm and 30 nm, following a quantitative analysis of the polarization- and spectrally-resolved extinction cross section on hundreds of individual nanoparticles. The measured cross sections were fitted using an ellipsoid model. By minimizing the fit error or the variation of the fitted dimensions with color channel selection, the material permittivity dataset and the surface damping parameter  $g$  best describing the nanoparticles are found to be the single crystal dataset by Olmon *et al.* [Phys. Rev. B **86**, 235147 (2012)] and  $g \approx 1$ , respectively. The resulting nanoparticle geometries are in good agreement with transmission electron microscopy of the same sample batches, including both 2D projection and tomography.

Published under license by AIP Publishing. <https://doi.org/10.1063/5.0031012>

## I. INTRODUCTION

With the increase in employment of nanoscale materials throughout the sciences, it has become an important issue to accurately assess the size and shape of nanoparticles (NPs), whether for research or industrial applications. Credible and robust

measurements of these parameters are also critical to comply with regulations. For NPs with dimensions well below the diffraction limit for visible light ( $\sim 250$  nm), the industry standard to accurately determine NP geometries is electron microscopy (EM). However, EM requires complex and expensive instrumentation and is time-consuming, which is a serious limitation, especially when

repeated statistical information on NP populations is required, for example, for synthesis development and quality control in NP manufacturing.

Notably, there has been increasing research interest in understanding the relationship between the optical properties of NPs, such as absorption and scattering of light, and the NP size and shape, especially for plasmonic nanosystems exhibiting a strong localized surface plasmon resonance (LSPR). Several methods have been reported to directly measure the NP optical scattering cross section<sup>2–4</sup>  $\sigma_{\text{sca}}$ , the absorption cross section<sup>5–7</sup>  $\sigma_{\text{abs}}$ , or their sum, the extinction cross section<sup>6,8,9</sup>  $\sigma_{\text{ext}}$ . A few studies also reported measurements of the real and imaginary parts of the NP polarizability.<sup>10,11</sup> Once these properties are known, by assuming a particular model for the geometry, it is possible to solve the inverse problem, namely, calculating the NP geometry from its polarizability. To realize this, the critical piece of connecting information is the complex material permittivity  $\epsilon$ . However,  $\epsilon$  is typically obtained by performing ellipsometry measurements on surfaces of bulk materials<sup>1,12,13</sup> rather than on NPs. Therefore, discrepancies arise to the effective  $\epsilon$  for NPs due to the spatial extension of the excitations responsible for the material polarization, also known as non-local effects.<sup>14,15</sup> These are specifically relevant for metals, where the conduction electron mean free path at room temperature is typically several tens of nanometers<sup>16</sup> and thus comparable to the NP size. The effect of the electrons experiencing an interface is often modeled as an additional damping of the free electron gas in the Drude model, called electron surface scattering.<sup>9,17</sup> This damping depends on the interface structure and the adjacent material so that in the literature, an increase in the damping for interfaces to strongly bound adjacent materials has been called chemical interface damping.<sup>18</sup>

The discrepancy between the permittivity measured by ellipsometry on surfaces of bulk materials and the effective permittivity of metallic NPs can lead to inaccuracies in the determination of the geometric properties from the measured optical properties, and vice versa. One would need to account for the discrepancy either through modeling, for example, via the addition of a damping term for surface scattering<sup>9,17,18</sup> to the imaginary part of the Drude model for conduction electrons in a solid, or through the use of the dielectric function measured directly from NPs, rather than bulk material. Measurements of the complex permittivity of single gold NPs of 10 nm and 15 nm size have been presented by Stoller *et al.*,<sup>10</sup> revealing that, in particular, for gold nanospheres (GNSs) with LSPR around 530 nm, the measured imaginary part deviates from that of the bulk significantly for wavelengths  $\lambda$  below 520 nm. However, it should be noted that the NPs used in that work (manufactured by British Biocell, now called BBISolutions) can vary greatly from the assumed spherical or even ellipsoidal shape as we have shown in Ref. 19. Khadir *et al.*<sup>11</sup> presented a direct measurement of single NP polarizabilities of gold nanospheres of nominal diameter,  $D = 100$  nm, and polystyrene beads of  $D = 200$  nm, from which one should be able to deduce  $\epsilon$ . In this case, the agreement with the measured bulk permittivity using the dataset of Johnson and Christy<sup>12</sup> was good, consistent with the rather large size of the NPs, above the mean-free path. In both cases, NP variability and reliance on nominal specifications limit the ability to present an accurate assessment of permittivity from the measured quantities.

Recently, our group published a technique, dubbed the optical nanosizer,<sup>19</sup> providing the three-dimensional (3D) shape and size of NPs by a comparison between the dipolar Rayleigh–Gans (ellipsoidal) model and measurements of  $\sigma_{\text{ext}}$  with polarization resolution and coarse spectral resolution. It should be noted that measurements of the individual components of  $\sigma_{\text{ext}}$ , namely,  $\sigma_{\text{sca}}$  and  $\sigma_{\text{abs}}$ , are not required, as  $\sigma_{\text{ext}}$  can be modeled directly as their sum. The method offers the ability to measure hundreds of NPs in a single field of view, with sensitivities below  $1 \text{ nm}^2$ , corresponding to the cross section of a  $D \approx 2$  nm GNS. Various nominally spherical and rod-shaped gold NPs were investigated. The 3D sizes and shapes obtained by the optical measurements on hundreds of NPs were compared with those obtained through EM on the same NP batches, including tomography. The optical nanosizer determined the diameter and anisotropy of the NPs with precision around 1 nm and 10%, respectively, and generally, good agreement was found with the results from the EM analysis.

Notably, one of the examined samples were GNSs with nominal  $D = 30$  nm, which exhibit extreme uniformity in both size and shape, with  $\hat{D}/D = \pm 4.5\%$ , where the accent ^ indicates the standard deviation of the quantity. In this case, comparison to EM revealed a small but noticeable discrepancy (beyond the error due to noise) between the mean diameters and aspect ratios (ARs) found by the two techniques, the origin of which remained somewhat unexplained in our previous work. Owing to the extreme uniformity of these NPs and the precision of our analysis method, we hypothesize that the observed discrepancy is linked to an incorrect description of the material permittivity. In this work, we have evaluated this hypothesis by changing the model to take into account different material permittivities, according to various datasets available in literature for gold, and by including a surface damping parameter in the Drude damping rate. We applied the revised model to the morphometric analysis of the  $D = 30$  nm ultra-uniform gold nanospheres (UGNSs) previously measured, and on a new dataset acquired on nominally  $D = 10$  nm UGNSs. A set of metrics was developed to robustly and consistently quantify the effects of changing the material permittivity and the surface damping parameter across hundreds of NPs. This study clearly identifies an optimum material permittivity dataset, notably different from the widely used one in the work of Johnson and Christy,<sup>12</sup> shedding light on this subtle yet consequential effect.

## II. PERMITTIVITY, POLARIZABILITY, AND THE OPTICAL CROSS SECTIONS OF NANOPARTICLES

The free electron contribution to the complex permittivity in metals is typically calculated using the Drude model. Additionally, bound electron contributions associated with the interband transitions from the  $d$  bands into the conduction band are important for gold, since they occur in the visible optical range for  $\lambda \lesssim 540$  nm, and overlap with the LSPR of spherical NPs. To describe the gold NP permittivity including surface damping, we use here an analytical model<sup>4,20</sup> given by

$$\epsilon_{\text{NP}} = 1 - \frac{\omega_{\text{p}}^2}{\omega(\omega + i\Gamma)} + \epsilon^{\text{b}}(\omega), \quad (1)$$

with  $\omega_p$  being the plasma frequency,  $\varepsilon^b$  being the contribution from the bound electrons,<sup>20,21</sup> and  $\Gamma$  being the Drude damping rate. To consider surface damping,  $\Gamma$  is approximated<sup>22</sup> by

$$\Gamma = \Gamma_0 + g \frac{v_F}{R}, \quad (2)$$

where  $R = D/2$  is the NP radius,  $\Gamma_0$  is the bulk damping rate,  $v_F = 1.4 \times 10^6$  m/s is the Fermi velocity in gold,<sup>16</sup> and  $g$  is a dimensionless number parameterizing the surface damping. A full set of the parameters used can be found in Table S1 of Ref. 4. Several experiments have been performed to measure  $\varepsilon$  of bulk gold. In this work, we refer to those of Johnson and Christy,<sup>12</sup> McPeak *et al.*,<sup>13</sup> and Olmon *et al.*<sup>1</sup> The former two performed spectroscopic ellipsometry on thin polycrystalline films of gold, while Olmon *et al.* included single crystalline gold. Values of  $g$  reported in the literature on gold NPs vary<sup>9,20</sup> typically between 0.2 and 2, and hence, we chose to explore this parameter space. For this work, Eq. (1) was used to fit each permittivity dataset independently for  $g = 0$ . The resulting models were then evaluated as a function of  $g$ , providing a series of different  $\varepsilon_{NP}$  to be used to determine the geometric properties of the NPs from the optical measurements. The resulting permittivities are given in Figs. 1(a) and 1(b) in the absence of surface damping ( $g = 0$ ) and for strong surface damping ( $g = 1.5$ ), for  $D = 10$  nm and 30 nm, showing that the surface damping mainly increases the imaginary part of the Drude permittivity  $\Gamma \omega_p^2 \omega^{-3} / (1 + \Gamma^2 / \omega^2)$ , proportional to the cube of the wavelength for  $\Gamma \ll \omega$ .

It is relevant at this point to introduce the polarizability, specifically that of the Rayleigh-Gans model, and to formally define the optical cross sections. The polarizability is determined by the material complex permittivity, the geometry of the NP, and the permittivity,  $\varepsilon_m$ , of the surrounding medium. For an ellipsoidal NP with three semi-axes ( $a, b, c$ ), we order the semi-axes such that  $a \geq b \geq c$  and choose a Cartesian reference system of unit vectors  $\hat{e}'_\kappa$ , with  $\kappa = x', y', z'$  pointing in the directions of  $a, b$ , and  $c$ , respectively. The polarizability tensor  $\alpha'$  is a diagonal matrix in this basis, whose entries are the polarizabilities for fields oriented along each of the semi-axes of the NP. The diagonal entries are given by

$$\alpha'_\kappa = V \varepsilon_0 \frac{\varepsilon_{NP} - \varepsilon_m}{\varepsilon_m + L_\kappa (\varepsilon_{NP} - \varepsilon_m)}, \quad (3)$$

with  $V$  being the NP volume,  $\varepsilon_0$  being the free-space permittivity,  $\varepsilon_m$  being the dielectric function of the surrounding medium, and  $L_\kappa$  being the depolarization factors. The  $L_\kappa$  are determined by the geometry of the NP, and for a sphere,  $L_\kappa = 1/3$ . We assume  $\varepsilon_m$  to be real and constant in frequency and assume both NP and medium to be non-magnetic, i.e., having unity relative permeability. For an incident field  $\vec{E}'$ , we have the induced electric dipole moment,

$$\vec{p}' = \alpha' \vec{E}'. \quad (4)$$

For NPs arbitrarily oriented,  $\alpha'$  must be transformed into the laboratory reference frame, defined by a Cartesian coordinate system with axes labeled  $i \in \{x, y, z\}$ , with unit vectors  $\vec{e}_i$ , where  $\vec{e}_z$  points along the optical path, and  $\vec{e}_x, \vec{e}_y$  span the sample plane.

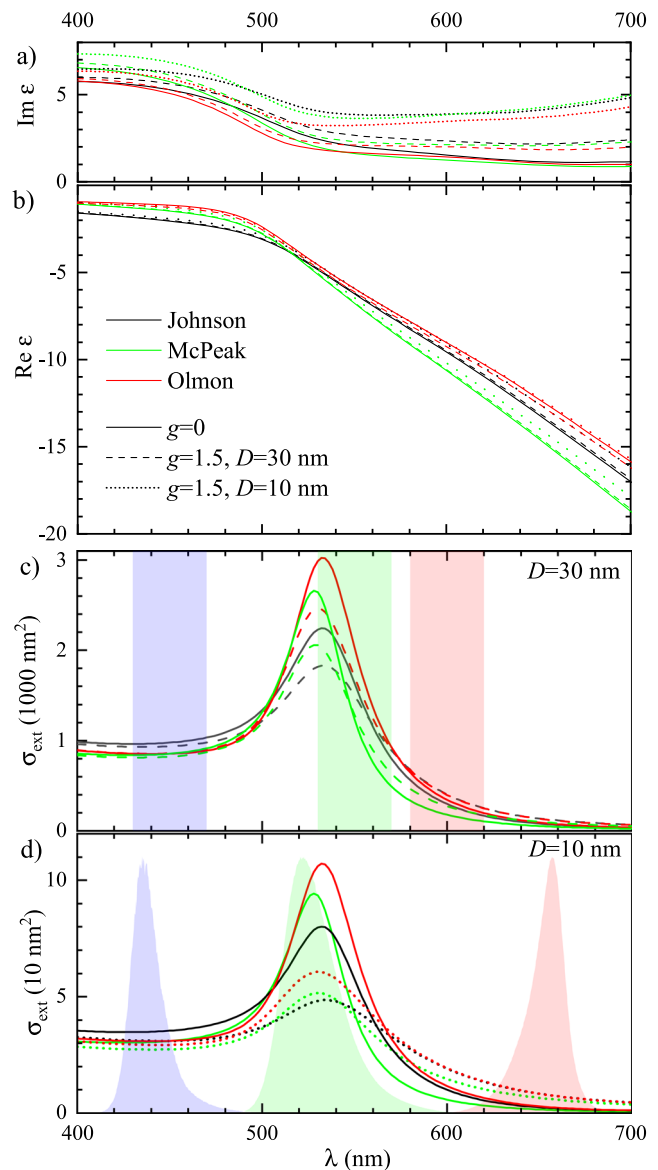


**FIG. 1.** (a) and (b) Permittivity of gold calculated with the model, as discussed in Refs. 4 and 20, fitted to the measured data of Johnson *et al.*,<sup>12</sup> Olmon *et al.*,<sup>1</sup> or McPeak *et al.*,<sup>13</sup> without ( $g = 0$ ) and with strong ( $g = 1.5$ ) surface damping for diameters of  $D = 10$  nm and 30 nm. (c) Corresponding extinction cross section of  $D = 10$  nm and 30 nm spheres in  $n = 1.52$  medium. (d) as (c) but for  $D = 10$  nm. The blue, green, and red color bands in (c) represent the passbands of the  $\Lambda = (450, 550, 600)$  nm color channels used in the  $D = 30$  nm UGNS measurements. The colored spectra in (d) are the LED illumination spectra of  $\Lambda = (450, 530, 660)$  nm used in the  $D = 10$  nm UGNS measurements.

We define the 3D rotation matrix (Ref. 19) using  $R = R_\psi R_\theta R_\phi$  and  $R^T = R_\phi^T R_\theta^T R_\psi^T$ , with  $\phi, \theta$ , and  $\psi$  being the angles of rotation about  $\vec{e}_x, \vec{e}_y$ , and  $\vec{e}_z$ , respectively. A vector  $\vec{v}'$  in the NP frame transforms into the laboratory frame as  $\vec{v} = R\vec{v}'$  so that Eq. (4) becomes

$R^T \vec{p} = \alpha' R^T \vec{E}$ , and we find that the polarizability in the laboratory frame is

$$\alpha = R \alpha' R^T. \quad (5)$$

The optical cross sections,  $\sigma_{\text{sca}}$  and  $\sigma_{\text{abs}}$ , are defined as the power scattered ( $P_{\text{sca}}$ ) or absorbed ( $P_{\text{abs}}$ ) from the incident field by the NP relative to the intensity,  $I_{\text{inc}}$ , of the incident field, so that  $\sigma_{\text{sca}} = P_{\text{sca}}/I_{\text{inc}}$  and  $\sigma_{\text{abs}} = P_{\text{abs}}/I_{\text{inc}}$ , respectively. In the electrostatic limit  $D \ll \lambda$ , the cross sections are related to  $\vec{p}$ , and hence  $\hat{\alpha}$ , via

$$\sigma_{\text{abs}}(\vec{E}) = \frac{k}{\epsilon_0} \frac{\text{Im}(\vec{E}^* \cdot \vec{p})}{|\vec{E}|^2} \quad (6)$$

and

$$\sigma_{\text{sca}}(\vec{E}) = \frac{k^4}{6\pi\epsilon_0^2} \frac{|\vec{p}|^2}{|\vec{E}|^2}, \quad (7)$$

where  $k = 2\pi n_m/\lambda$  is the wavenumber in the medium of refractive index,  $n_m = \sqrt{\epsilon_m}$ , and the star denotes complex conjugation.

The calculated  $\sigma_{\text{ext}}$  for  $D = 30$  nm and  $D = 10$  nm GNSs ( $R = a = b = c = D/2$ ) are given in Figs. 1(c) and 1(d), respectively, for models fitting the three measured permittivities without surface damping ( $g = 0$ ) or with a strong surface damping ( $g = 1.5$ ). The surface damping is more significant for the smaller GNSs, as follows from Eq. (2), broadening the LSPR and thus lowering the peak and increasing  $\sigma_{\text{ext}}$  at longer wavelengths.

### III. EXPERIMENT

The experimental setup and data analysis are described in detail in Ref. 19. We give here a summary and the details relevant to the samples studied in this work.

#### A. Optical measurements

The optical transmission measurements were performed using a Nikon Ti-U inverted microscope, with illumination provided by either a 100 W tungsten halogen lamp with bandpass filters (center wavelengths of 450 nm, 550 nm, and 600 nm) of 40 nm width or a light emitting diode (LED) source (Thorlabs LED4D106) with three independent LEDs of center wavelengths 455 nm, 530 nm, and 660 nm coupled via a liquid light guide (Thorlabs AD5LLG). The excitation spectra are shown in Figs. 1(c) and 1(d). Light was focused onto the sample with a 1.34 numerical aperture (NA) oil-immersion condenser (Nikon MEL41410), limited to either 0.95 NA or 1.00 NA, and collected by either a 0.95 NA 40 $\times$  dry objective (Nikon MRD00405) or a 1.45 NA 100 $\times$  oil objective (Nikon MRD01905), respectively, both in conjunction with a 1.5 $\times$  tube lens. A linear polarizer before the condenser controlled the excitation polarization angle  $\gamma_p$ . The image data were recorded using a scientific-CMOS (sCMOS) camera (PCO Edge 5.5) capable of acquiring 100 frames/s at 2560  $\times$  2160 pixel<sup>2</sup> and a full-well capacity of  $N_{\text{fw}} = 30\,000$  electrons. The illumination intensities and exposure times were chosen to result in pixel values close to  $N_{\text{fw}}$  without entering the range of non-linear response.

#### B. Samples and their preparation for optical measurements

NPs branded as “ultra-uniform GNSs” of nominal spherical shape and mean diameter of 10 nm and 30 nm were obtained from NanoComposix. Glass slides and coverslips (Menzel Gläser, No. 1.5) were cleaned by sequential sonication steps in toluene to remove non-polar substances, in acetone to clear the toluene, and then rinsed and boiled in deionized (DI) water. Slides and coverslips were then left in 30% hydrogen peroxide for at least 24 h, allowing oxidation of remaining surface contaminants, as well as hydrophilizing the glass surfaces. It is notable that this protocol offers a reasonable substitute for the much more hazardous “Piranha” etch, often used to clean glass for similar applications. Prior to NP deposition, any required glass was washed with DI water. The NP colloid was diluted with water to a final concentration of 10<sup>8</sup> NP/ml, and a volume of 200  $\mu$ l was spin-coated onto the coverslips at 2000 rpm for 2 min, with an acceleration time of 30 s. This procedure provided a homogeneous density of NPs over the surface of the coverslip of (0.1–0.4) NP/ $\mu$ m<sup>2</sup> such that most NPs visible in the image are resolved individuals with well-separated point spread functions (PSFs). The NP side of the coverslip was coated in 18  $\mu$ l of refractive index  $n = 1.52$  silicone oil and covered with a slide. The samples were pressed and sealed with clear nail varnish.

#### C. Measurement of extinction

We use a method to quantitatively measure  $\sigma_{\text{ext}}$ , which has been described in detail in Ref. 23. Briefly, two *brightfield* images called  $I_1$  and  $I_2$  are obtained, differing by a lateral shift of the sample by a few optical resolutions, and averaged over a number,  $N_i$ , of individual acquisitions, to reduce shot noise. Two extinction images are then obtained as  $\Delta_{1,2} = 1 - I_{1,2}/I_{2,1}$ , respectively. To further reduce shot noise while simultaneously reducing the systematic noise due to sensor electronic drift, we average the extinction over a number of repetitions  $N_r$ . The extinction cross section of a NP centered in an area  $A_{1,2}$  of radius  $r_i$  in  $I_{1,2}$ , respectively, is calculated as  $2\sigma_{\text{ext}} = \int_{A_1} \Delta_1 dA + \int_{A_2} \Delta_2 dA$ . The shot-noise-limited standard deviation in the measurement of  $\sigma_{\text{ext}}$  is then given by<sup>23</sup>

$$\hat{\sigma}_{\text{ext}} = \frac{r_i d_{\text{px}}}{M} \sqrt{\frac{\pi}{N_a N_{\text{fw}}}}, \quad (8)$$

with the magnification  $M$  from sample to detector, the number of acquired frames  $N_a = N_i N_r$ , and  $d_{\text{px}} = 6.5$   $\mu$ m being the pixel pitch of the sensor. We use  $r_i = 3\lambda/(2NA)$  unless otherwise stated. For typical values of  $N_i = 128$  and  $N_r = 4$ ,  $\hat{\sigma}_{\text{ext}}$  is about 50 nm<sup>2</sup> and measurements are shot-noise limited, with increasing  $N_a$ , down to  $\hat{\sigma}_{\text{ext}}$  of about 4 nm<sup>2</sup>. Below this value, surface roughness, debris, and/or residual sensor fluctuations affect the results for our setup and samples. These settings are sufficient for the  $D = 30$  nm UGNSs, which have  $\sigma_{\text{ext}}$  in the 10<sup>3</sup> nm<sup>2</sup> range.

For the  $D = 10$  nm UGNSs, which have  $\sigma_{\text{ext}}$  in the few 10 nm<sup>2</sup> range, we instead use a method described in Sec. IV B of Ref. 23, which allows us to achieve  $\hat{\sigma}_{\text{ext}}$  down to 1 nm<sup>2</sup>. Briefly, we reduce the measurement area to the minimum possible by analyzing  $\Delta_1$

via Wiener deconvolution and hence taking into account the effect of shifted referencing. For  $\Delta_1 \ll 1$ , the response in the Fourier domain is  $h(\vec{k}) = -2i \sin(\vec{k} \cdot \vec{d}/2)$ , with  $\vec{d}$  being the shift vector in real space and  $\vec{k}$  being the wavevector. The deconvolution is performed by multiplying  $\Delta_1$  by  $f = 1/[h + 1/(\zeta h^*)]$ , with  $\zeta$  being an estimated signal-to-noise ratio (SNR) of the data. We use  $\zeta = 1$  and measure the cross sections directly from the peak values. The pixel values themselves are calibrated in units of  $\sigma_{\text{ext}}$  by measuring  $\sigma_{\text{ext}}$  of a strong absorber/scatterer with the method mentioned above. Here, we used 60 nm GNSs added to the sample at lower concentration.

When measuring  $\sigma_{\text{ext}}$  as a function of the excitation polarizer angle  $\gamma_p$ , we fit the data with

$$\sigma(\gamma_p) = \sigma \{1 + \alpha \cos[2(\gamma_p - \gamma)]\} \quad (9)$$

to extract the average given by  $\sigma$ , the polarization dependence given by the relative amplitude parameter  $\alpha > 0$ , and the angle  $\gamma \in [0, \pi)$  of maximum  $\sigma_{\text{ext}}$ .  $\alpha$  is a measure of the observed NP asymmetry, with  $\alpha = 0$  corresponding to absence of dipolar asymmetry.  $\gamma$  gives the observed orientation of the NP dipolar asymmetry in the sample plane. We denote the measured extinction cross section for a certain color channel  $\Lambda$  and polarizer orientation  $\gamma_p$  by  $\sigma_\Lambda(\gamma_p)$ .

#### D. Structural characterization

Transmission electron microscopy (TEM) was performed on a JEOL-JEM 2100 TEM operating at 200 kV, with samples prepared on 300 mesh hole-y carbon. High-angle annular dark-field scanning transmission electron microscope (HAADF-STEM) images and tomography series were acquired using a FEI Osiris microscope operated at 200 kV. The tomography series were acquired over the tilt range of  $\pm 75^\circ$  with a tilt increment of  $3^\circ$  using a Fischione 2020 single-tilt tomography holder and a pixel dwell time of 6  $\mu\text{s}$ . After alignment of the projection images via a cross correlation, the stacks of aligned projection images served as inputs for 20 iterations of the expectation-maximization reconstruction algorithm implemented in the ASTRA toolbox 1.9.0 using Matlab 2019a.<sup>24,25</sup> Amira 5.4.0 was used for the 3D rendering reported in Fig. 8.

### IV. RESULTS AND DISCUSSION

#### A. Statistical distributions of $\sigma_\Lambda$ and $\alpha_\Lambda$

The distribution of  $\alpha_\Lambda$  vs  $\sigma_\Lambda$  is shown in Fig. 2 for the two UGNS sizes, together with batch-representative TEM images. We call the mean of the polarization-averaged cross sections for a given color channel  $\bar{\sigma}_\Lambda$  and the associated standard deviation  $\hat{\sigma}_{\Lambda,m}$ . The analogous quantities of the  $\alpha$  distribution are called  $\bar{\alpha}_\Lambda$  and  $\hat{\alpha}_{\Lambda,m}$ . For each NP, we determine the error of the fitted parameters  $\sigma$ ,  $\alpha$ , and  $\gamma$  using a Monte Carlo-like simulation, as detailed in Ref. 19. Briefly, we add random Gaussian noise to the measured data, matching the experimentally determined noise for each  $\gamma_p$  and  $\Lambda$ , refit the data, and use the standard deviation of the resulting parameter distribution as error. Let us denote the standard deviation of the per-NP fitted parameter  $\sigma_i$  by  $\hat{\sigma}_{\Lambda,i}$ , where  $i$  numbers the  $N$  NPs. We

then define  $\hat{\sigma}_\Lambda = \sqrt{\hat{\sigma}_{\Lambda,m}^2 - \frac{1}{N} \sum_{i=1}^N \hat{\sigma}_{\Lambda,i}^2}$ , which represents the distribution of NP cross sections across the various NPs only due to their different sizes and shapes, having subtracted the contribution from measurement noise. Note that for  $\hat{\alpha}_{\Lambda,m}$ , this correction has not been done, since the corresponding standard deviations  $\hat{\alpha}_{\Lambda,i}$  vary strongly depending on  $\hat{\alpha}_{\Lambda,m}$  and  $\bar{\sigma}_\Lambda$ , and we use  $\hat{\alpha}_\Lambda = \hat{\alpha}_{\Lambda,m}$ .

Figure 2(a) presents the measured  $\sigma_\Lambda$  and  $\alpha_\Lambda$  of a set of  $D = 30$  nm UGNSs, which exhibit narrow distributions of both  $\sigma_\Lambda$  and  $\alpha_\Lambda$ . We find  $\alpha_{600}$  to be below 0.2 (apart from some outliers accounting for 4.7% of the population) with a mean and standard deviation  $\bar{\alpha}_{600} \pm \hat{\alpha}_{600} = 0.058 \pm 0.031$ , indicating NPs of very low ellipticity.  $\hat{\sigma}_{450}/\bar{\sigma}_{450}$  and  $\hat{\sigma}_{550}/\bar{\sigma}_{550}$  are both about 18%. For NPs much smaller than the wavelength,  $\sigma_{\text{ext}}$  is roughly proportional to the NP volume  $V$ , and hence, 18% relative volume distribution corresponds to 6% radius distribution.  $\hat{\sigma}_{600}/\bar{\sigma}_{600}$  is larger, about 41%, consistent with the fact that the variability of  $\sigma_{\text{ext}}$  at a wavelength above the LSPR of a spherical NP is sensitive to deviations from the spherical shape, with elliptical shapes resulting in a red-shifted LSPR. This can be seen in the correlation of increasing  $\sigma_{600}$  with  $\alpha_{600}$  for the outliers having larger deviations from the spherical shape in Fig. 2(a). Notably, correlating  $\sigma_{600}$  with  $\sigma_{550}$  (see inset), two groups can be identified, with different ratios  $\sigma_{600}/\sigma_{550}$  identifying two distinct shapes. The ratio 0.21, indicated by the dashed line, is attributed to a shape close to the spherical shape, while the ratio of 0.85, indicated by the dotted line, is consistent<sup>19</sup> with an oblate shape with  $c/a \approx 0.7$ . Qualitatively, these observations are consistent with TEM [see Fig. 2(a), right], where most NPs are defect-free, as indicated by the homogeneous contrast in the bright-field TEM images, and have a close to spherical shape, but some contain defects and are clearly non-spherical. We find that  $\bar{\sigma}_{550} > \bar{\sigma}_{450} > \bar{\sigma}_{600}$  as expected for spherical gold NPs with a LSPR at  $\lambda \approx 530$  nm in a homogeneous environment of the  $n = 1.52$  refractive index [see Fig. 1(c)].

Figure 2(b) presents the measured  $\sigma_\Lambda$  and  $\alpha_\Lambda$  of a set of  $D = 10$  nm UGNSs. The cross sections of these NPs are much smaller, in the 50 nm<sup>2</sup> range, so that we used a larger number of repetitions  $N_r = (16, 16, 46)$  for the LED illumination with  $\Lambda = (455, 530, 660)$  nm, reducing the noise to  $\hat{\sigma}_{\text{ext}} = (4.5, 6.5, 3.7)$  nm<sup>2</sup>. Considering the measured  $\bar{\sigma}_\Lambda = (20.4, 47.6, 5.3)$  nm<sup>2</sup>, the SNR is (4.5, 7.4, 1.4). Notably, for  $D = 30$  nm and associated  $\Lambda$ , the SNR is (10.5, 20.8, 8), considerably higher than for the 10 nm UGNSs, despite the larger  $N_r$  used in the latter case. For  $\Lambda = 530$  nm (the channel having the highest SNR), we find  $\bar{\alpha}_{530} \pm \hat{\alpha}_{530} = 0.092 \pm 0.067$  and  $\hat{\sigma}_{530}/\bar{\sigma}_{530} = 24\%$  and, hence, estimate the relative radius distribution to be about  $\sim 8\%$  so that these UGNSs exhibit slightly broader distributions of both  $\sigma_\Lambda$  and  $\alpha_\Lambda$  compared to the  $D = 30$  nm nanoparticles. The other color channels have a SNR too small for a similar analysis. Correlating  $\sigma_{660}$  with  $\sigma_{530}$  (see the left inset), we find that  $\sigma_{660} \approx 0.12 \sigma_{530}$ . The lower factor arises from the 60 nm red shift of the  $\Lambda = 660$  channel compared to  $\Lambda = 600$  channel used for the  $D = 30$  nm UGNSs. Qualitatively, these observations are consistent with TEM, where most of the NPs are defect-free and have a round slightly faceted shape, while a few NPs contain defects and hence vary from these shapes, as shown for a few red outliers in Fig. 2(b). Note that  $\alpha_{660}$  has a significant noise, as indicated by the gray area, so that for most NPs, its SNR is less than one, as also seen in the right inset where no correlation between  $\alpha_{660}$  and  $\alpha_{530}$  is observed.

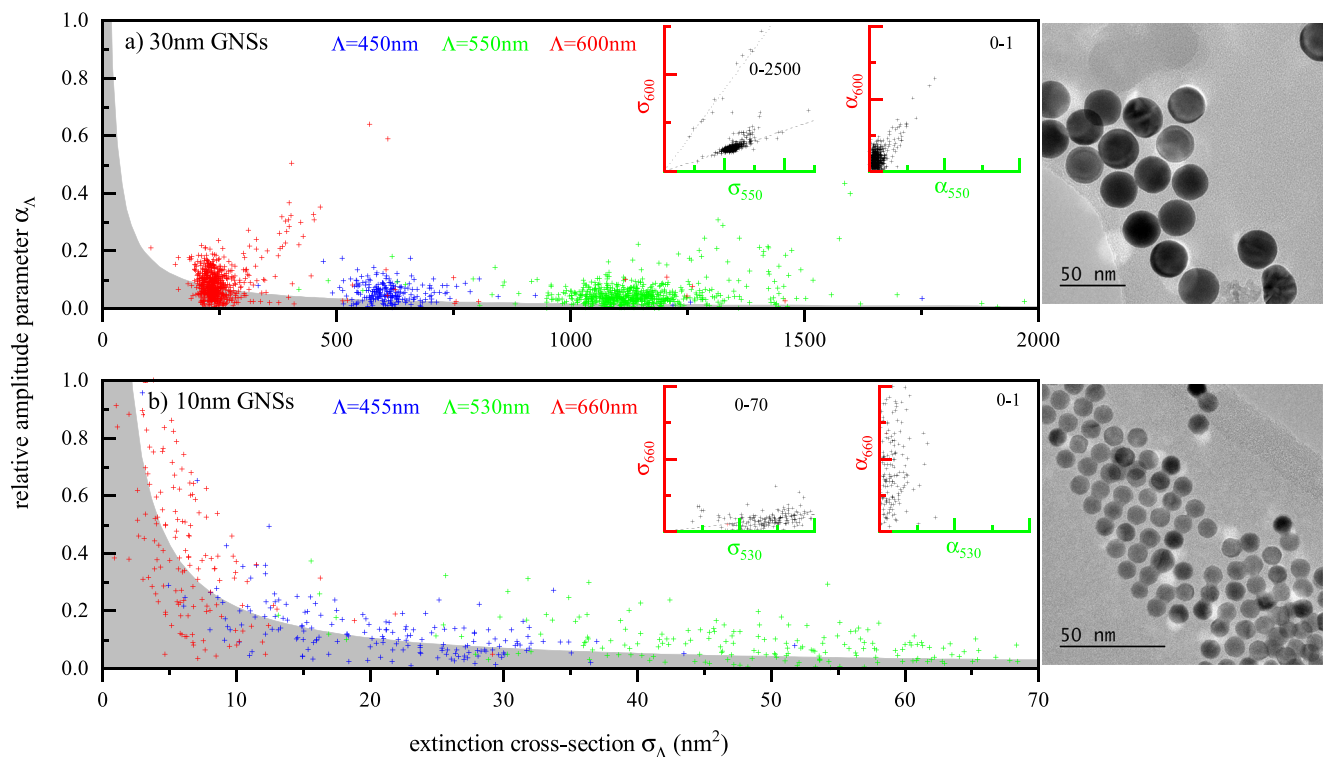


**FIG. 2.** Asymmetry  $\alpha_\Lambda$  vs cross section  $\sigma_\Lambda$  for sets of different NPs and channels  $\Lambda$  as given, with representative TEM images of the investigated NP batch on the right. In all cases,  $N_i = 128$ . The gray areas indicate the noise in the fitted  $\alpha$  of the red channels due to  $\hat{\sigma}_{\text{ext}}$  estimated as  $(\hat{\sigma}_{\text{ext}}/\sqrt{3})/\sigma_\Lambda$ . (a)  $N = 223$   $D = 30$  nm GNSs using  $NA = 0.95$  and  $N_r = (4, 4, 16)$  for  $\Lambda = (450, 550, 600)$ , yielding  $\hat{\sigma}_{\text{ext}} = (57.5, 53.1, 30.9)\text{nm}^2$ . Left inset:  $\sigma_{600}$  vs  $\sigma_{550}$ . The dashed line shows  $\sigma_{600} = 0.21\sigma_{550}$ , and the dotted line  $\sigma_{600} = 0.85\sigma_{550}$ . Right inset:  $\alpha_{600}$  vs  $\alpha_{550}$ . Both on a range as indicated. (b) GNSs with  $N = 180$  and  $D = 10$  nm using  $NA = 1.45$  and  $N_r = (16, 16, 46)$  for  $\Lambda = (455, 530, 660)$ , yielding  $\hat{\sigma}_{\text{ext}} = (4.5, 6.5, 3.7)\text{nm}^2$ . Left inset:  $\sigma_{660}$  vs  $\sigma_{530}$ . The dashed line shows  $\sigma_{660} = 0.12\sigma_{530}$ . Right inset:  $\alpha_{660}$  vs  $\alpha_{530}$ . Both on a range as indicated. The 30 nm data are also shown in Ref. 19, replicated here for convenience.

## B. Morphometric analysis

The morphometric analysis method, solving the inverse problem, is discussed in detail in Ref. 19. Briefly,  $\sigma_{\text{sca}}$  and  $\sigma_{\text{abs}}$  are calculated over a grid in the multidimensional parameter space  $b/a$ ,  $c/a$ ,  $\phi$ ,  $\theta$ , and  $\psi$ , taking into account the illumination intensity spectra of the color channels  $\Lambda$  and the selected permittivity (see Fig. 1). Interpolants are created for  $\sigma_{\text{sca}}$  and  $\sigma_{\text{abs}}$  from the values on the grid. Then, for each parameter set on the grid, the measured values are compared to the calculated values using the normalized error,

$$S^2 = \frac{1}{N} \sum_{\gamma_p, \Lambda} \left( \frac{\sigma_\Lambda(\gamma_p) - \sigma_{\text{abs}, \Lambda}(\gamma_p) - \eta \sigma_{\text{sca}, \Lambda}(\gamma_p)}{\hat{\sigma}_\Lambda(\gamma_p)} \right)^2, \quad (10)$$

where  $N$  is the number of measurements in the experiment and  $\hat{\sigma}_\Lambda(\gamma_p)$  is the measurement noise associated with  $\sigma_\Lambda(\gamma_p)$ . Only a fraction  $\eta$  of  $\sigma_{\text{sca}}$  is measured, since the objective collects light from a finite solid angle, and thus, some of the light scattered by the NP is collected. For our experimental configuration, we calculated  $\eta = 0.864$ .<sup>19</sup> The right side of Eq. (10) is a fourth-order polynomial in  $V$  so that we can minimize  $S^2$  vs  $V$  using the analytical roots of

the third-order algebraic equation  $\frac{d}{dV} S^2 = 0$  to obtain  $S$  and  $V$  for the specific dataset and determine a volume-equivalent diameter,  $D_V = \sqrt[3]{6V/\pi}$ . All points on the grid with  $S^2$  smaller than a certain cutoff are used as initial guesses for a gradient descent using the  $\sigma_{\text{sca}}$  and  $\sigma_{\text{abs}}$  interpolants. Hence, for every NP under examination, there can be multiple solutions, and we choose the parameter set with the minimum  $S^2$  over all solutions as the one best describing the size, shape, and orientation of the NP. Prior knowledge, such as ensemble size specifications from the NP manufacturer, can also be taken into account and used to apply a penalty according to the variation of the retrieved parameters from the nominal specifications. We perform this operation as a post-fit sorting and selection routine and use

$$S_c^2 = S^2 + \frac{1}{3} \sum_{i \in \{D_V, b/a, c/a\}} \left( \frac{p_i - \bar{p}_i}{\hat{p}_i} \right)^2, \quad (11)$$

with the mean,  $\bar{p}_i$ , and the standard deviation,  $\hat{p}_i$ , obtained from TEM for the parameters  $p_i$ ,  $i \in \{D_V, b/a, c/a\}$ , to determine the best parameter set as the one with minimum  $S_c^2$ .

In this work, we want to examine the effect of  $\varepsilon_{\text{NP}}$  on the fit results. We choose to consider three quantities to act as a figure of merit (FOM) for  $\varepsilon_{\text{NP}}$ . The first follows naturally from the analytical methodology described above. We observe the effect of  $\varepsilon_{\text{NP}}$  on  $S$ , specifically calculating

$$\bar{S} = \sqrt{M\{S^2\}}, \quad (12)$$

where  $M\{\cdot\}$  indicates that we take the median of the quantity over the  $N$  NPs analyzed. Taking the median instead of the mean is more robust to outliers. In Eq. (10), we normalize the difference between the experiment and the model by  $\hat{\sigma}_{\text{ext}}(\gamma_p)$  so that for the correct model, we expect  $S = 1$ . However, since in our case, we have for each NP six free parameters and 18 measurements  $[\sigma_{\Lambda}(\gamma_p)]$  for six different  $\gamma_p$  and three different  $\Lambda$ , the number of fit parameters is a significant fraction of the number of values to be fitted, and thus, the parameters will be able to partially fit the noise. In a simple estimation, we expect a value of  $S \approx \sqrt{(18-6)/18} \approx 0.81$ .

The second FOM is the median of the penalized error,

$$\bar{S}_c = \sqrt{M\{S_c^2\}}, \quad (13)$$

which takes into account the prior knowledge from TEM, and is a combined agreement with the measurements and the morphology measured by TEM. In contrast to  $S$ , the value of  $S_c$  can be much larger than 1, the case in which it is dominated by the applied penalty. For a correct model and TEM morphology parameters, we expect  $\bar{S}_c \approx \sqrt{2}$  due to the sum of the two normalized variances in Eq. (11).

The third FOM evaluates the consistency of the fitted geometry using different combinations of color channels. Since the wavelength dependence of the model is given mostly by the permittivity, for close-to-spherical NPs, and the NP geometry is independent of wavelength, using the correct permittivity should result in a constant retrieved shape independent of the color channels used, apart from effects of measurement noise. Therefore, the more consistent the NP geometry is between color channel combinations, the better the permittivity describes the NPs.

We have therefore refitted the measured data using each of the three possible combinations of two out of three  $\Lambda$ , which we number with the index  $\ell \in \{1, 2, 3\}$ , e.g., for  $D = 30$  nm, we have  $\{450, 550\}$  nm,  $\{450, 600\}$  nm, and  $\{550, 600\}$  nm. This results in fit parameters  $p_{\ell,i}$  for the  $\ell$ th  $\Lambda$  combination. We then define the deviation between the fit with the combination  $\ell$  and the fit using all three  $\Lambda$  as

$$s = \sqrt{\frac{1}{9} \sum_{\ell=1}^3 \sum_{i \in \{D_V, b/a, c/a\}} \left( \frac{p_{\ell,i} - p_i}{A_i} \right)^2}, \quad (14)$$

with the normalizing factor  $A_i = D_V, 1, 1$ , using  $D_V$  from the three  $\Lambda$  fit. We define the FOM as a median of the  $s_j$  over the  $N$  NPs,

$$\bar{s} = M\{s\}, \quad (15)$$

providing a measure of the average NP size and shape parameter deviation for fits using two  $\Lambda$  from the one using all three  $\Lambda$ .

The resulting figures of merit are shown in Fig. 3 as a function of the surface damping parameter  $g$  for each of the experimental  $\varepsilon$

datasets from the work of Johnson and Christy,<sup>12</sup> McPeak *et al.*,<sup>13</sup> and Olmon *et al.*<sup>1</sup> Looking first at  $\bar{S}$ , we find that the minimum value is about 0.73, close to the estimated value due to the measurement noise. The lowest values are achieved for the Olmon dataset

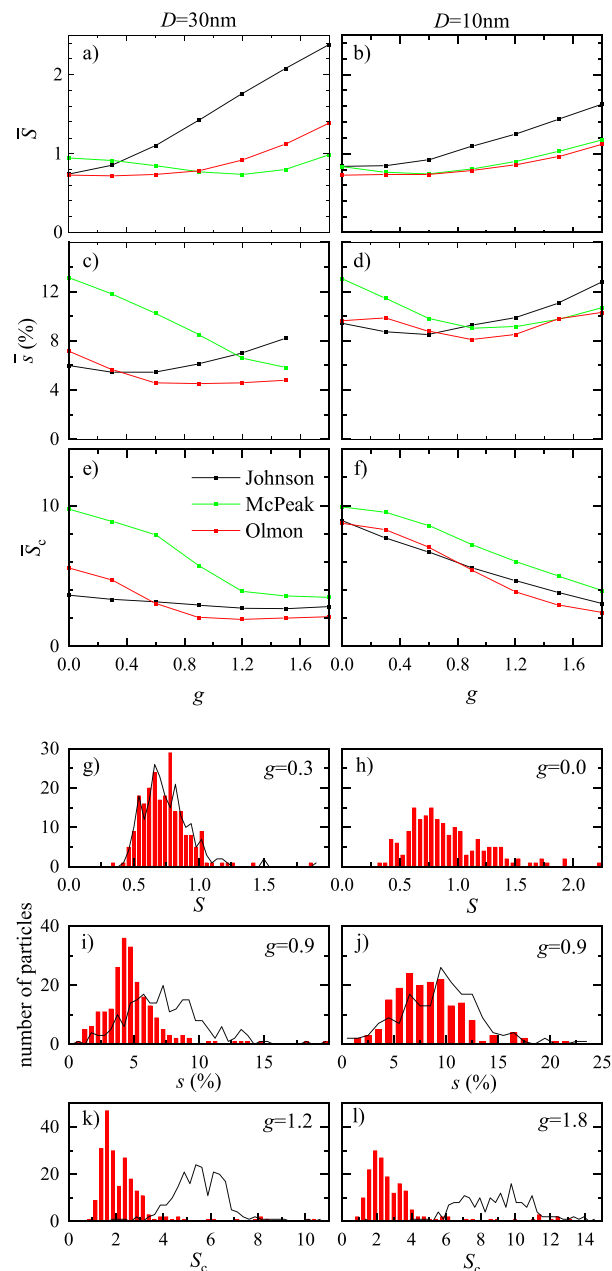


**FIG. 3.** FOM and statistics for UGNs of  $D = 30$  nm (left column) and  $D = 10$  nm (right column). [(a) and (b)]  $\bar{S}$ , [(c) and (d)]  $\bar{s}$ , and [(e) and (f)]  $\bar{S}_c$  vs  $g$ , with colors indicating the  $\varepsilon$  dataset used. (g)–(l) are histograms using the Olmon dataset. [(g) and (h)]  $S$  with  $g$  minimizing  $\bar{S}$ . The black line shows the case  $g = 0$ . (i) and (j) as (g) and (h) but for  $s$  with  $g$  minimizing  $\bar{s}$ . (k) and (l) as (g) and (h) but  $S_c$  with  $g$  minimizing  $\bar{S}_c$ .



for both UGNS sizes.  $\bar{S}$  is rather insensitive to the value of  $g$ , with a range of 0–1 within 10% of the minimum  $\bar{S}$ . The measurements thus indicate that  $\epsilon_{\text{NP}}$  is best described by the Olmon dataset with a surface damping  $g$  up to about 1. The histograms of  $S$  are shown in Figs. 3(g) and 3(h) for Olmon and  $g = (0.3, 0.0)$ , for which  $\bar{S}$  is minimum, and for comparison for  $g = 0$  (line). We find a close-to-normal distribution for both sizes, with a weak tail of high  $S$  values representing outlier shapes not captured by the model. There is little difference for the two  $g$ , consistent with weak dependence of  $\bar{S}$  on  $g$ .

Next, we consider  $\bar{s}$ , which shows again a minimum for the Olmon dataset but is more sensitive to  $g$ . For  $D = 30$  nm, there is a minimum at  $g = 0.9$ , where  $\bar{s} = 4.5\%$ , and a range within 10% of the  $\bar{s}$  minimum for  $g$  between 0.5 and 1.5. For  $D = 10$  nm, the situation is similar, with a minimum at  $g = 0.9$ , where  $\bar{s} = 7.8\%$ , and a range within 10% of the minimum for  $g$  between 0.6 and 1.3. The larger minimum value of  $\bar{s}$  is attributed to the lower SNR for the  $D = 10$  nm measurements, providing a less precise retrieval of the size and shape, specifically for the two-channel results. Importantly, the results of  $\bar{s}$  and  $\bar{S}$  are compatible

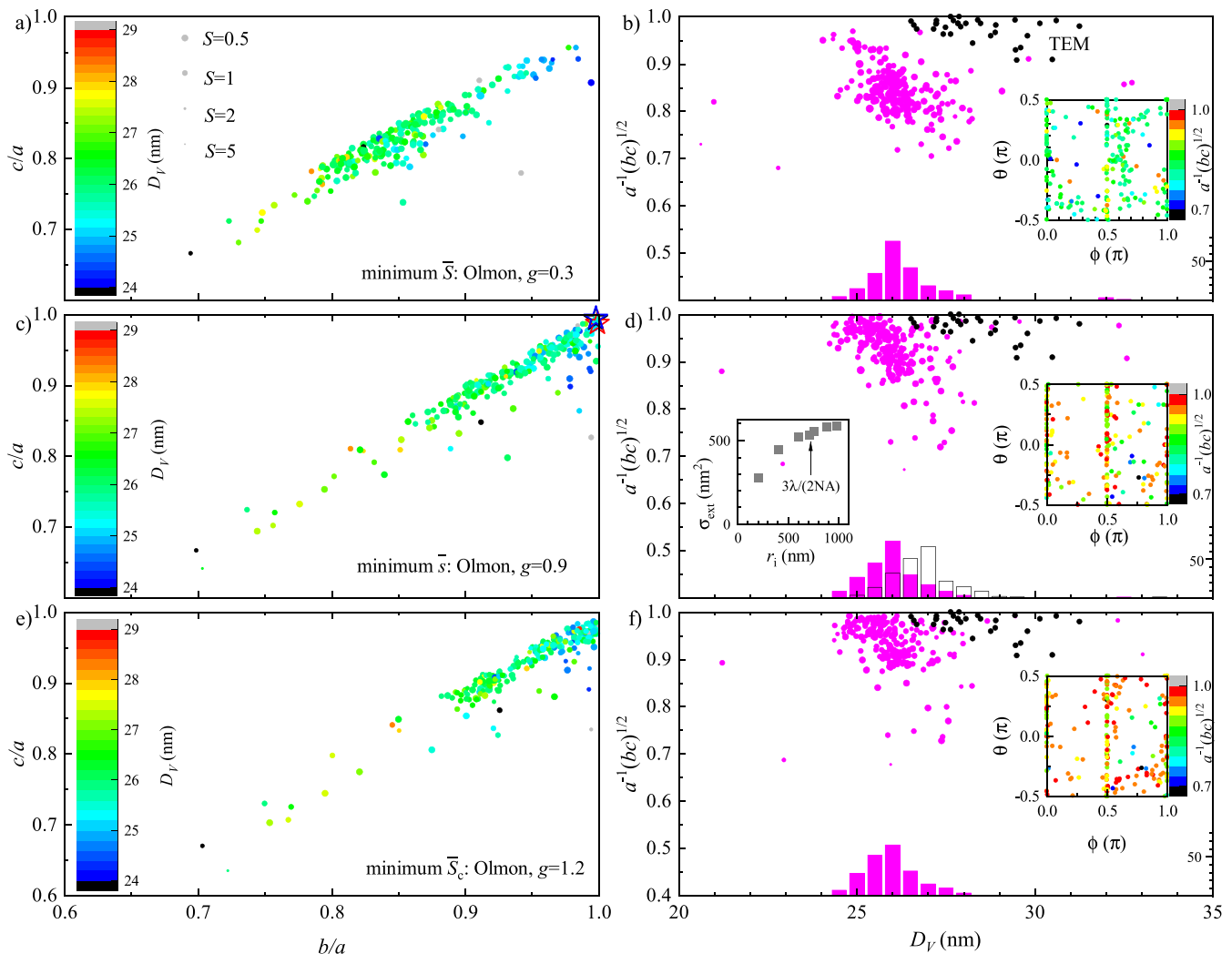


**FIG. 4.** Fit results for UGNSs with  $N = 223$  and  $D = 30$  nm when using [(a) and (b)] Olmon with  $g = 0.3$  minimizing  $\bar{S}$ , [(c) and (d)] Olmon with  $g = 0.9$  minimizing  $\bar{s}$ , and [(e) and (f)] Olmon  $g = 1.2$  minimizing  $\bar{S}_c$ . The left column shows the ARs with a color indicating the fitted diameter  $D_V$ . The right column shows the average AR parameter  $\sqrt{bc}/a$  as a function of  $D_V$ , with the histogram showing the number distribution of  $D_V$ . The black points indicate TEM measurements, where we have assumed  $b = c$ . Insets indicate the pitch ( $\theta$ ) and roll ( $\phi$ ) angles determined from the fit to show the out of plane orientation ( $\phi, \theta \neq 0$ ). The size of the fit datapoints in (a)–(f) is given by  $S^{-1} = 1/(1 + S)$  and represents the fit error with larger points indicating lower error. In (d), an additional retrieved histogram of  $D_V$  is shown as black outline bars, resulting when correcting the measured  $\sigma_{\text{ext}}$  by a factor 1.105, compensating the finite  $r_1 = 3\lambda/(2\text{NA})$  used in the analysis. The dependence of the measured  $\sigma_{\text{ext}}$  on  $r_1$  for  $\Lambda = 450$  nm averaged over 39 NPs is shown in the left inset.

and indicate that for both sizes,  $\epsilon_{NP}$  is described well by the Olmon dataset with  $g = 0.9$ . Comparing the different datasets, we see that for  $D = 30$  nm, the dependence  $\bar{S}(g)$  for Johnson is similar to  $\bar{S}(g + 1)$  for Olmon. Considering that Johnson refers to polycrystalline films, while Olmon refers to monocrystalline, it appears that the difference can be attributed to the additional surface damping by a crystallite size on the order of 30 nm. McPeak instead shows results less compatible between  $\bar{S}$  and  $\bar{s}$  and between the two UGNS sizes. It features a stronger Drude contribution, as shown by the steeper slope of  $\text{Re } \epsilon$  toward the longer wavelength in Fig. 1(b) and by the higher plasma frequency in the model parameters (see Table S1 of Ref. 4).

The histograms of  $s$  are shown in Figs. 3(i) and 3(j) for Olmon and  $g = 0.9$ , for which  $\bar{s}$  is minimum, and for comparison for

$g = 0$  (line). We find a rather broad distribution for both UGNS sizes, again with a weak tail of high  $s$  values representing outlier shapes not captured by the model. In contrast to the histograms of  $S$ , there is a significant difference for the two  $g$ , consistent with the stronger dependence of  $\bar{s}$  on  $g$ . The broad distribution is attributed to the sensitivity of the cross sections to variations of the shape parameters, as shown in Ref. 19.

Finally, we consider  $\bar{S}_c$ , which is the only FOM where prior knowledge on the size and shape distribution is used. We find again that the Olmon dataset is the best suited one. For  $D = 30$  nm, there is a minimum at  $g = 1.2$ , where  $\bar{S}_c$  is about 1.9, and a range within 10% of the minimum for  $g$  between 0.8 and 1.8. This result is compatible with the one of  $\bar{s}$  and  $\bar{S}$ , indicating that the ellipsoidal model is well suited to describe most of the NP shapes. For

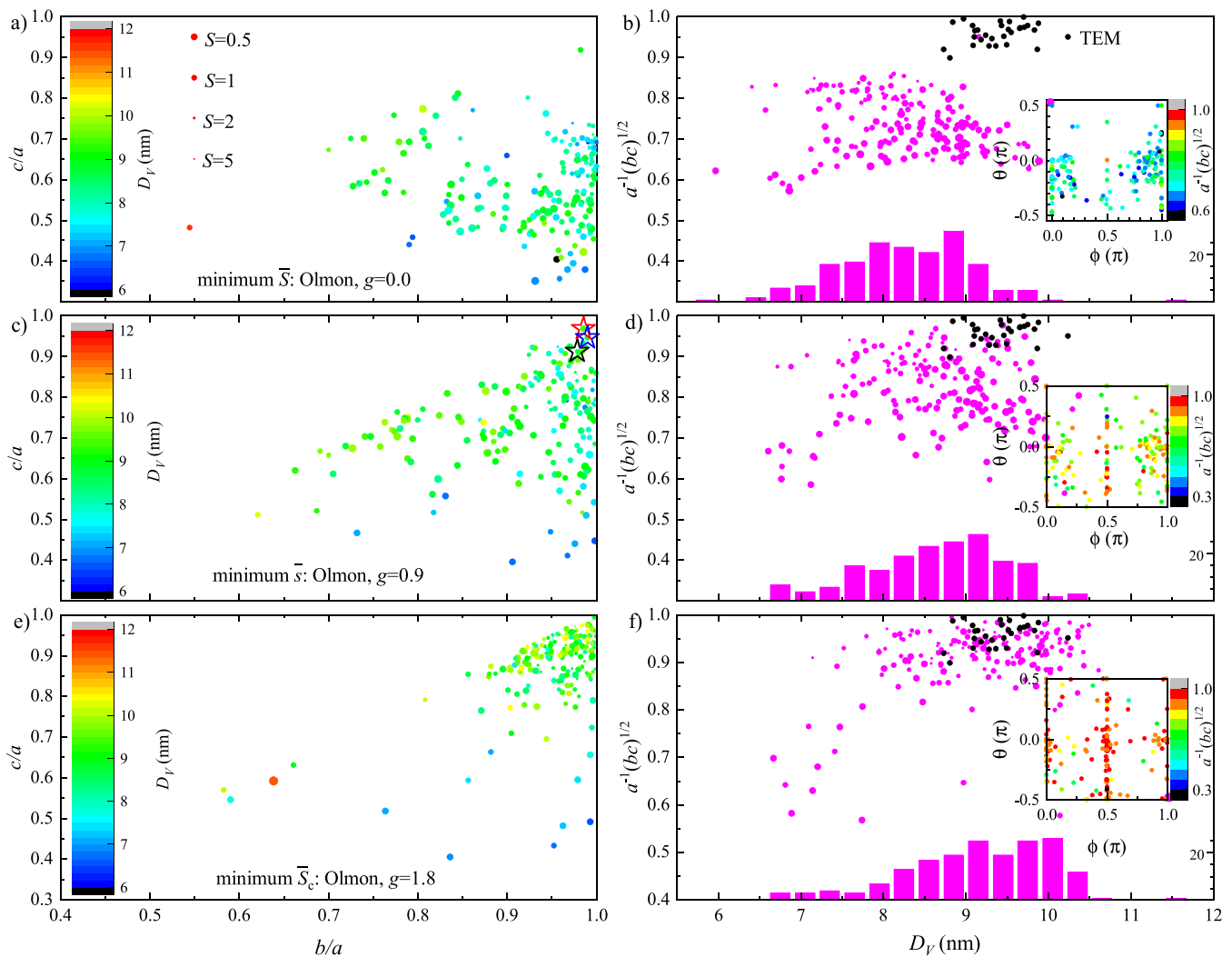


**FIG. 5.** As Fig. 4 but for UGNSs with  $N = 179$  and  $D = 10$  nm using [(a) and (b)] Olmon  $g = 0.3$  minimizing  $\bar{S}$ , [(c) and (d)] Olmon  $g = 0.9$  minimizing  $\bar{s}$ , and [(e) and (f)] Olmon  $g = 1.8$  minimizing  $\bar{S}_c$ .

$D = 10$  nm, however, the minimum occurs for  $g \geq 1.8$ , deviating significantly from the range given by  $\bar{S}$  and  $\bar{s}$ . This finding is attributed to the lower SNR in these data, resulting in systematic errors in the retrieved shape due to the intricate dependence of the simulated cross sections on the shape parameters, as will be detailed below.

The optimum value of the surface damping  $g$  around 1 found in the present work is consistent with previous reports<sup>4,17</sup> on NPs. In view of the influence of the surface chemistry on  $g$  reported in Ref. 18, it is worthwhile to mention that, in the investigated UGNs, PEG-carboxyl is covalently bound to the surface of the NPs.

In Fig. 4, we show the results of the morphometric fit for the individual NPs in the case of UGNs with  $D = 30$  nm for the Olmon

dataset and  $g$  minimizing  $\bar{s}$ ,  $\bar{S}$ , or  $\bar{S}_c$ . We find that most retrieved NPs shapes are prolate, as shown in the left column by the clustering close to the diagonal  $a > b \approx c$ . For  $g = 0.3$  minimizing  $\bar{S}$ , the averaged AR  $\sqrt{bc}/a$  is around 0.82 [see Fig. 4(b)], while for  $g = 0.9$  minimizing  $\bar{s}$ , this increases to about 0.9 [see Fig. 4(d)], and for  $g = 1.2$  minimizing  $\bar{S}_c$ , it does not change significantly. Notably, the higher AR is compatible with the TEM data. The angle distributions (see the inset in the right column) are rather similar for the three values of  $g$ .

There is still a small systematic deviation between the diameter  $D_V$  determined by the optical sizing and the one seen in TEM [solid circles in Fig. 4(d)], with the former about 2 nm–3 nm smaller on average. Importantly, the noise in the data does not give rise to a systematic error in  $D_V$ , as demonstrated in Fig. 6 of Ref. 19.

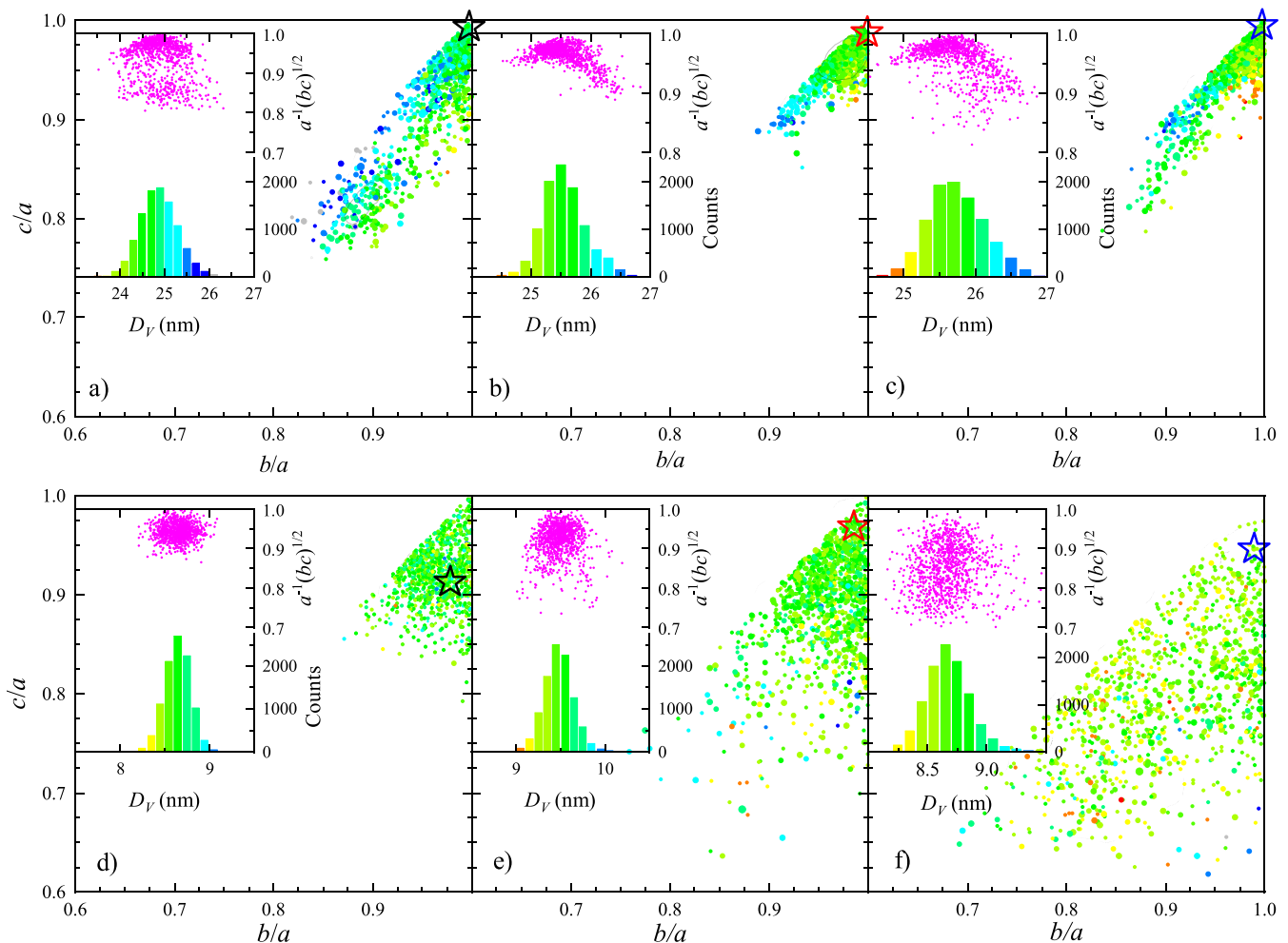


**FIG. 6.** For the measured NPs indicated by stars in Figs. 5(c) and 4(c), fit results for 10 000 realizations (1000 shown by filled circles) of added random measurement noise using the Olmon dataset with  $g = 0.9$ . Contours are the boundaries of regions of the highest density containing 68% (black) and 95% (gray) of the data. Insets show the distributions of  $D_V$  and provide the symbol color scale and the AR (magenta). The NPs of the 30 nm UGNs in panels (a)–(c) have  $\alpha_{550} = (0.016, 0.033, 0.023)$  and  $\sigma_{550} = (1166, 1223, 1233)$  nm<sup>2</sup>, and the NPs of the 10 nm UGNs in (d)–(f) have  $\alpha_{530} = (0.049, 0.025, 0.128)$  and  $\sigma_{530} = (57.3, 61.7, 46.0)$  nm<sup>2</sup>.

Therefore, this deviation should be attributed to systematic errors in the measurement or the modeling. A known systematic in the evaluation of the cross section is the usage of a finite area, not completely capturing  $\sigma_{\text{ext}}$ . We have discussed this in Ref. 23—using a smaller area improves the SNR and allows for measurement of denser NP arrangements. We have analyzed the dependence of  $\sigma_{\text{ext}}$  on  $r_i$  for  $\Lambda = 450$ , an average over 39 NPs, which had sufficient separation from other NPs, as shown in the left inset of Fig. 4(d). We find a factor of 1.105 between  $r_i = 742 \text{ nm} \approx 3\lambda/(2\text{NA})$  and the maximum  $r_i = 979 \text{ nm}$  analyzed, limited by the lateral shift used in the measurements. The dependence on  $r_i$  appears to saturate at this value. Taking this factor into account, the resulting  $D_V$  histogram [given in Fig. 4(d) as the black outline] exhibits an increase in the  $D_V$  from  $(26.0 \pm 1.1) \text{ nm}$  to  $(26.9 \pm 1.1) \text{ nm}$ , consistent with the volume scaling of  $\sigma_{\text{ext}}$ . This reduces the systematic deviation to 1 nm–2 nm, smaller than size distribution. This is a remarkable accuracy given that it depends on the theoretical model and the measurement of the absolute cross sections.

In Fig. 5, the results for the  $D = 10 \text{ nm}$  UGNs are shown. We find that the retrieved NP shape is more broadly distributed in both  $b/a$  and  $c/a$ , as well as in diameter. These broadened distributions are mostly related to the measurement noise. For  $g = 0.0$  minimizing  $\bar{S}$ , the shape tends to be more oblate, with ARs spread between 0.6 and 0.9. For  $g = 0.9$  minimizing  $\bar{s}$ , a random ellipsoidal shape is found, with ARs spread between 0.7 and 1.0. The diameter  $D_V$  is spread between 7 nm and 10 nm, which is not dominated by the measurement noise, as we will see below. For  $g = 1.8$  minimizing  $\bar{S}_c$ , the ARs are pushed toward the spherical shape, more consistent with the TEM data, as expected for this FOM. Notably, the large  $g$  results in higher cross sections for  $\Lambda = 660$  so that the fit is biased to avoid non-spherical shapes, which would further increase this cross section.

Unlike the retrieved size  $D_V$ , the shape does acquire a significant systematic error due to measurement noise for close-to-spherical NPs, as was demonstrated in Fig. 6 of Ref. 19. Indeed, the spherical shape is at the corner of the two-dimensional shape parameter space  $1 \geq b/a \geq c/a > 0$ , and any noise can only result in non-sphericity. To evaluate the effect in the present data, three close-to-spherical NPs were selected from each of the 10 nm and 30 nm UGNs, indicated by stars in Figs. 5(c) and 4(c). Random Gaussian noise of standard deviation  $\hat{\sigma}_{\text{ext}}$  was added to the experimental data, and the NP parameters were retrieved from the resulting data using the Olmon dataset with  $g = 0.9$ . This was repeated for 10 000 noise realizations, and the results are shown in Fig. 6. The contours indicate the regions of highest probability density containing 68% and 95% of the data, which, for a Gaussian distribution, are the  $\sigma$  and  $2\sigma$  confidence intervals, respectively.

The results for the 30 nm UGNs in Figs. 6(a)–6(c) show that the measurement noise results in about 1 nm full width at half maximum (FWHM) in  $D_V$ , which is about half the width of the distribution shown in Fig. 4(d). The retrieved  $D_V$  distribution is thus affected by the noise but still represents the NP size distribution well. Looking at the shape parameters  $b/a$  and  $c/a$ , the different NPs show quite different results. Figure 6(a) shows a bimodal distribution, with a maximum close to spherical, and a smaller peak around  $b/a = 0.9$  and  $c/a = 0.82$ . Such multimodal distributions arise from the complex fitting landscape over NP

rotation and shape.<sup>19</sup> In Fig. 6(b), instead, the shape is close to spherical, with  $b/a \approx 0.97$  and  $c/a \approx 0.95$ . Finally, Fig. 6(c) shows a distribution intermediate between the ones in (a) and (c). The measured shape distribution [Figs. 4(c) and 4(d)] is therefore strongly influenced by the measurement noise. While NPs with retrieved ARs below 0.8 cannot be explained by the noise and thus are certainly non-spherical, the majority of the NPs have retrieved ARs above 0.9 and would be consistent with a spherical shape within the measurement noise.

For the 10 nm UGNs shown in Figs. 6(d)–6(f), the noise results in about 0.5 nm FWHM in  $D_V$ , which is well below the width of the distribution of about 2 nm FWHM shown in Fig. 5(d). The width of the NP distribution is therefore not significantly influenced by the noise. Also here, the three selected NPs show different shape distributions, generally more widely spread due to the lower SNR of the data. The shape is spread between spherical and  $b/a \geq 0.85$  and  $c/a \geq 0.7$  and an AR above 0.8. The measured shape distribution [Figs. 5(c) and 5(d)] is therefore significantly influenced by the measurement noise—however, NPs having a retrieved AR below 0.75 cannot be explained by the noise and thus are non-spherical.

### C. Tomography

HAADF-STEM tomography was performed on the UGNs to characterize the morphology of the NPs. Examples of two  $D = 30 \text{ nm}$

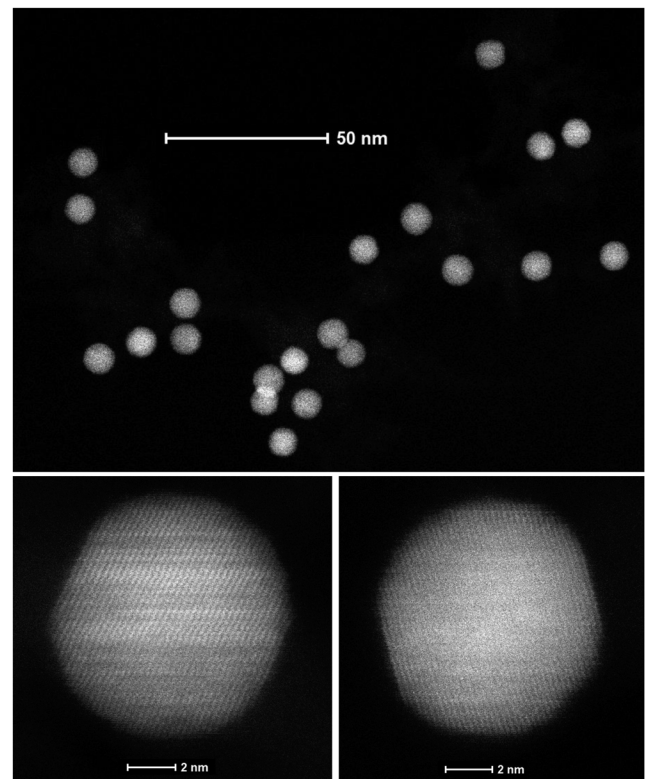
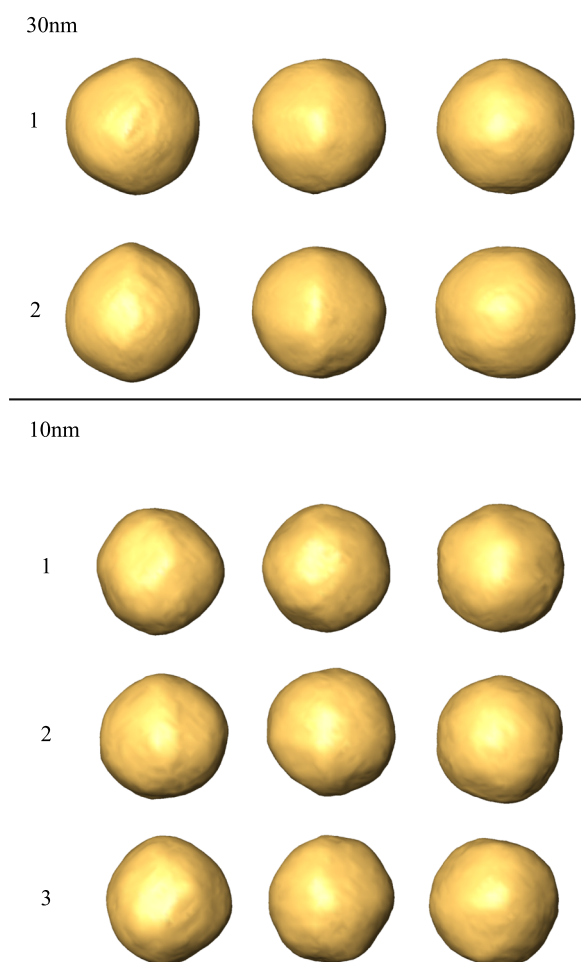


FIG. 7. STEM images of  $D = 10 \text{ nm}$  UGNs.

and three  $D = 10$  nm UGNs, shown in Fig. 8, exhibit largely defect-free (as established from the STEM images, see Fig. 7) and show faceting. The resulting volumes and ARs are given in Table I. ARs determined from both the 2D projection and the 3D reconstruction are close to one for all five UGNs. The statistics resulting from HAADF-STEM measurements of 61  $D = 30$  nm and 126  $D = 10$  nm UGNs are shown in Table II. Both species are highly monodisperse in both  $D$  and AR, with  $\widehat{D}/\overline{D} = 6.3\%$  and  $\widehat{AR}/\overline{AR} = 2.4\%$  for the  $D = 30$  nm NPs and  $\widehat{D}/\overline{D} = 3.76\%$  and  $\widehat{AR}/\overline{AR} = 2.94\%$  for the  $D = 10$  nm NPs. This can be compared with the corresponding results from the optical characterization,  $\widehat{D}_V/\overline{D}_V = 5.1\%$  for the 30 nm and  $\widehat{D}_V/\overline{D}_V = 22\%$  for the 10 nm UGNs. While the 30 nm result is consistent with tomography, the 10 nm result shows a much larger size distribution. The measurement noise corresponds to about 1% for the 30 nm and 3% for the 10 nm UGNs and does not dominate the findings. Since the STEM statistics from Table II were not obtained not using tomography, but 2D projection images, there is a possibility that some of the 10 nm UGNs are flattened,



**FIG. 8.** 3D tomographic reconstructions of two  $D = 30$  nm UGNs (top)<sup>19</sup> and three  $D = 10$  nm UGNs (bottom). Each NP is visualized over the same three planes ( $xy$ ,  $xz$ , and  $yz$ ). The volumes and ARs of each NP can be found in Table I.

**TABLE I.** Measured NP volume and AR for the NPs from Fig. 8. A comparison is made between the measured ARs obtained from the 3D reconstruction and the corresponding 2D projection image of the same NP. The ARs were calculated by dividing the length of two orthogonal lines through the middle orthoslice (3D) or the projection image (2D).

NP	Volume ( $10^3$ nm <sup>3</sup> )	AR from 3D	AR from 2D
30 nm—1	13.10	0.99	0.98
30 nm—2	12.10	0.96	1.00
10 nm—1	0.472	1.00	1.00
10 nm—2	0.492	0.99	0.99
10 nm—3	0.491	0.98	0.94

**TABLE II.** HAADF-STEM derived mean and standard deviation of parameters  $p_i$ . Here, we consider the two main semi-axes seen in the 2D projection and assign the longer to  $a$  and the shorter to  $b$  and  $c$ .

NP type	$\bar{p}_{D_V} \pm \hat{p}_{D_V}$ (nm)	$\bar{p}_{b/a} \pm \hat{p}_{b/a}$
$D = 30$ nm	$28.73 \pm 1.81$	$0.973 \pm 0.024$
$D = 10$ nm	$9.556 \pm 0.359$	$0.962 \pm 0.031$

not visible in plane-view STEM but in the optical measurements. Another aspect to be considered is that faceting of NPs depends on their environment and so might change between vacuum (TEM) and oil (optical measurements). Specifically, for the small 10 nm NPs, the surface facets (see Fig. 7) might have a significant influence on the optical response. Additionally, electron-beam induced reshaping might also play a role.

## V. CONCLUSIONS

In summary, we have reported an in-depth quantitative analysis of the effects of using three gold permittivity datasets from the literature, and a surface damping parameter varying from 0 to 1.8, when fitting experimentally measured optical extinction cross sections of hundreds of individual gold nanoparticles. Quantitative measurements of the cross section magnitude were performed as a function of the incident light polarization direction and for three color channels. The samples investigated were ultra-uniform, mostly defect-free, nominally spherical NPs of 30 nm and 10 nm diameter, exhibiting a very narrow size and shape distribution, which enabled us to unravel the effects of permittivity and surface damping, without being affected by the dispersity of the sample. To determine the permittivity dataset and damping parameters best reproducing the measured cross sections consistently across hundreds on NPs, we introduced three figures of merit, namely, (i) the median of the fit error across the population of NPs analyzed, (ii) the median of a so-called penalized error using prior knowledge of the NP morphometric parameters from TEM, and (iii) the average size and shape parameter deviation for fits using two wavelength combinations compared to three. The smallest figures of merit were found consistently when using the gold permittivity dataset published by Olmon *et al.*<sup>1</sup> rather than the widely used one from the study of Johnson and

Christy.<sup>12</sup> The dependence of the figures of merit on the damping parameter indicated that  $g \approx 1$  describes the data across both sizes. Nanoparticle sizes and shapes obtained by solving the inverse problem with this permittivity compared well with in-plane TEM and tomography analysis, taking into account the measurement precision and accuracy. This study exemplifies the capabilities of optical studies for morphological and compositional analysis of NPs, providing an alternative tool complementing electron microscopy.

## AUTHORS' CONTRIBUTION

L.M.P., W.L., and P.B. conceived the work. L.M.P. prepared the samples for the optical measurements and performed the related measurements and data analysis. W.A. prepared the samples for the STEM tomography and performed the related measurements and data analysis. L.M.P., P.B., and W.L. developed the numerical model and fitting methods. L.M.P. performed the numerical simulations and data fitting. F.M. calculated the modified permittivity datasets. A.Z. calculated the relative field strengths in the illumination. All authors contributed to the data interpretation and writing of the manuscript.

## ACKNOWLEDGMENTS

This work was supported by the Welsh Government Life Sciences Bridging Fund (Grant No. LSBF/R6-005), the UK EPSRC (Grant Nos. EP/I005072/1 and EP/M028313/1), and the European Commission (Grant No. EUSMI E191000350). P.B. acknowledges the Royal Society for her Wolfson research merit award (Grant No. WM140077). F.M. acknowledges the Ser Cymru II programme (Case ID 80762-CU-148) which is part-funded by Cardiff University and the European Regional Development Fund through the Welsh Government. W.A. acknowledges an Individual Fellowship from the Marie Skłodowska-Curie actions (MSCA) under the EU's Horizon 2020 program (Grant No. 797153, SOPMEN) and Sara Bals for supporting the STEM measurements. The bright-field TEM was performed by Thomas Davies at Cardiff University. We acknowledge Iestyn Pope for technical support of the optical equipment.

## DATA AVAILABILITY

Information on the data underpinning the results presented here, including how to access them, can be found in the Cardiff University data catalog at <http://doi.org/10.17035/d.2020.0124374417>.

## REFERENCES

- <sup>1</sup>R. L. Olmon, B. Slovick, T. W. Johnson, D. Shelton, S.-H. Oh, G. D. Boreman, and M. B. Raschke, "Optical dielectric function of gold," *Phys. Rev. B* **86**, 235147 (2012).
- <sup>2</sup>A. Crut, P. Maioli, N. Del Fatti, and F. Vallée, "Optical absorption and scattering spectroscopies of single nano-objects," *Chem. Soc. Rev.* **43**, 3921–3956 (2014).
- <sup>3</sup>L. M. Payne, W. Langbein, and P. Borri, "Polarization-resolved extinction and scattering cross-section of individual gold nanoparticles measured by wide-field microscopy on a large ensemble," *Appl. Phys. Lett.* **102**, 131107 (2013).

- <sup>4</sup>A. Zilli, W. Langbein, and P. Borri, "Quantitative measurement of the optical cross sections of single nano-objects by correlative transmission and scattering microscopy," *ACS Photonics* **6**, 2149–2160 (2019).
- <sup>5</sup>D. Boyer, P. Tamarat, A. Maali, B. Lounis, and M. Orrit, "Photothermal imaging of nanometer-sized metal particles among scatterers," *Science* **297**, 1160–1163 (2002).
- <sup>6</sup>M. Husnik, S. Linden, R. Diehl, J. Niegemann, K. Busch, and M. Wegener, "Quantitative experimental determination of scattering and absorption cross-section spectra of individual optical metallic nanoantennas," *Phys. Rev. Lett.* **109**, 233902 (2012).
- <sup>7</sup>A. Tcherniak, J. W. Ha, S. Dominguez-Medina, L. S. Slaughter, and S. Link, "Probing a century old prediction one plasmonic particle at a time," *Nano Lett.* **10**, 1398–1404 (2010).
- <sup>8</sup>A. Arbouet, D. Christofilos, N. Del Fatti, F. Vallée, J. R. Huntzinger, L. Arnaud, P. Billaud, and M. Broyer, "Direct measurement of the single-metal-cluster optical absorption," *Phys. Rev. Lett.* **93**, 127401 (2004).
- <sup>9</sup>O. L. Muskens, P. Billaud, M. Broyer, N. Del Fatti, and F. Vallée, "Optical extinction spectrum of a single metal nanoparticle: Quantitative characterization of a particle and of its local environment," *Phys. Rev. B* **78**, 205410 (2008).
- <sup>10</sup>P. Stoller, V. Jacobsen, and V. Sandoghdar, "Measurement of the complex dielectric constant of a single gold nanoparticle," *Opt. Lett.* **31**, 2474–2476 (2006).
- <sup>11</sup>S. Khadir, D. André, P. C. Chaumet, S. Monneret, N. Bonod, M. Käll, A. Sentenac, and G. Baffou, "Full optical characterization of single nanoparticles using quantitative phase imaging," *Optica* **7**, 243–248 (2020).
- <sup>12</sup>P. B. Johnson and R. W. Christy, "Optical constants of noble metals," *Phys. Rev. B* **6**, 4370–4379 (1972).
- <sup>13</sup>K. M. McPeak, S. V. Jayanti, S. J. P. Kress, S. Meyer, S. Iotti, A. Rossinelli, and D. J. Norris, "Plasmonic films can easily be better: Rules and recipes," *ACS Photonics* **2**, 326–333 (2015).
- <sup>14</sup>N. A. Mortensen, S. Raza, M. Wubs, T. Søndergaard, and S. I. Bozhevolnyi, "A generalized non-local optical response theory for plasmonic nanostructures," *Nat. Commun.* **5**, 3809 (2014).
- <sup>15</sup>T. Christensen, W. Yan, A.-P. Jauho, M. Soljačić, and N. A. Mortensen, "Quantum corrections in nanoplasmonics: Shape, scale, and material," *Phys. Rev. Lett.* **118**, 157402 (2017).
- <sup>16</sup>D. Gall, "Electron mean free path in elemental metals," *J. Appl. Phys.* **119**, 085101 (2016).
- <sup>17</sup>C. Voisin, N. Del Fatti, D. Christofilos, and F. Vallée, "Ultrafast electron dynamics and optical nonlinearities in metal nanoparticles," *J. Phys. Chem. B* **105**, 2264–2280 (2001).
- <sup>18</sup>B. Foerster, A. Joplin, K. Kaefer, S. Celiksoy, S. Link, and C. Sönnichsen, "Chemical interface damping depends on electrons reaching the surface," *ACS Nano* **11**, 2886–2893 (2017).
- <sup>19</sup>L. M. Payne, W. Albrecht, W. Langbein, and P. Borri, "The optical nanosizer—Quantitative size and shape analysis of individual nanoparticles by high-throughput widefield extinction microscopy," *Nanoscale* **12**, 16215–16228 (2020).
- <sup>20</sup>F. Masia, W. Langbein, and P. Borri, "Measurement of the dynamics of plasmons inside individual gold nanoparticles using a femtosecond phase-resolved microscope," *Phys. Rev. B* **85**, 235403 (2012).
- <sup>21</sup>M. Guerrisi, R. Rosei, and P. Winsemius, "Splitting of the interband absorption edge in Au," *Phys. Rev. B* **12**, 557–563 (1975).
- <sup>22</sup>C. Voisin, D. Christofilos, P. A. Loukakos, N. D. Fatti, F. Vallée, J. Lermé, M. Gaudry, E. Cottancin, M. Pellarin, and M. Broyer, "Ultrafast electron-electron scattering and energy exchanges in noble-metal nanoparticles," *Phys. Rev. B* **69**, 195416 (2004).
- <sup>23</sup>L. M. Payne, W. Langbein, and P. Borri, "Wide-field imaging of single-nanoparticle extinction with sub-nm<sup>2</sup> sensitivity," *Phys. Rev. Appl.* **9**, 034006 (2018).
- <sup>24</sup>T. K. Moon, "The expectation-maximization algorithm," *IEEE Signal Process. Mag.* **13**, 47–60 (1996).
- <sup>25</sup>W. van Aarle, W. J. Palenstijn, J. De Beenhouwer, T. Altantzis, S. Bals, K. J. Batenburg, and J. Sijbers, "The ASTRA toolbox: A platform for advanced algorithm development in electron tomography," *Ultramicroscopy* **157**, 35–47 (2015).